Electric and magnetic dipole strength in ^{54}Fe

R. Schwengner[1], R. Massarczyk,[2] R. Beyer,[1] M. Bhike,[3,4] B. A. Brown,[5] Krishichayan,[3,4] K. Sieja,[6,7] W. Tornow,[3,4]
D. Bemmerer,[1] M. Butterling,[1] V. Derya,[8] M. Dietz,[1] F. Fiedler,[1] U. Friman-Gayer,[9,*] A. Frotscher,[1,†] M. Grieger,[1]
A. Hartmann,[1] A. R. Junghans,[1] T. Kögler,[1,10] F. Ludwig,[1] B. Lutz,[1] H. Pai,[11] T. Szücs,[1] M. P. Takács,[1,‡] and A. Wagner[1]

[1]*Helmholtz-Zentrum Dresden-Rossendorf, 01328 Dresden, Germany*
[2]*Los Alamos National Laboratory, Los Alamos, New Mexico 87545, USA*
[3]*Department of Physics, Duke University, Durham, North Carolina 27708, USA*
[4]*Triangle Universities Nuclear Laboratory, Durham, North Carolina 27708, USA*
[5]*National Superconducting Cyclotron Laboratory and Department of Physics and Astronomy,*
Michigan State University, East Lansing, Michigan 48824, USA
[6]*Université de Strasbourg, IPHC, 67037 Strasbourg, France*
[7]*CNRS, UMR7178, 67037 Strasbourg, France*
[8]*Institut für Kernphysik, Universität zu Köln, 50937 Köln, Germany*
[9]*Institut für Kernphysik, Technische Universität Darmstadt, 64289 Darmstadt, Germany*
[10]*OncoRay–National Center for Radiation Research in Oncology, Faculty of Medicine and University Hospital Carl Gustav Carus,*
Technische Universität Dresden, 01062 Dresden, Germany
[11]*Nuclear Physics Division, Saha Institute of Nuclear Physics, Kolkata-700064, India*

The dipole strength of the $N = 28$ closed-shell nuclide ^{54}Fe was studied in photon-scattering experiments using bremsstrahlung produced with electron beams of kinetic energies of 7.5 and 13.9 MeV at the γELBE facility as well as using quasimonoenergetic and linearly polarized photon beams of 26 different energies within the range from 5.5 to 11.4 MeV at the HIγS facility. About 100 $J = 1$ states were newly identified, out of them 19 with 1^+ and 30 with 1^- assignments. The quasicontinuum of unresolved transitions was included in the analysis of the spectra and the intensities of branching transitions were estimated on the basis of simulations of statistical γ-ray cascades. As a result, the photoabsorption cross section up to the neutron-separation energy was determined and compared with predictions of the statistical reaction model. The experimental $M1$ strengths from resolved 1^+ states are compared with results of large-scale shell-model calculations.

I. INTRODUCTION

The experimental and theoretical descriptions of photonuclear reactions and the inverse radiative-capture reactions are crucial for the understanding of particular astrophysical processes of element synthesis. An important ingredient to the calculations of reaction cross sections within the statistical reaction model is photon strength functions, which describe average transition strengths in the energy region of the quasicontinuum of nuclear states at high excitation energies. The standard electric dipole strength functions used in statistical

reaction-model calculations are Lorentz functions adjusted to (γ, n) reaction data that represent the isovector giant dipole resonance (GDR) [1]. To test whether the low-energy tail of the Lorentz approximation describes the strength function below the neutron-separation energy (S_n) correctly, experiments using other reactions are needed, in which nuclear levels below the particle-separation energies are excited [2].

A specific reaction for the study of dipole excitations up to the particle thresholds is photon scattering (γ, γ'), also called nuclear resonance fluorescence (NRF), in which the angular momentum $L = 1$ is predominantly transferred by the incident photons and states with spins and parities of $J^\pi = 1^+$ and 1^- are excited from the ground state in an even-even nucleus. Energy-integrated scattering cross sections of the excited states are determined from the intensities of the respective γ transitions back to the ground state and are used to determine reduced transition strengths for electric dipole ($E1$) and magnetic dipole ($M1$) transitions.

In recent photon-scattering studies using broad-band bremsstrahlung at the γELBE facility [3] of the Helmholtz-Zentrum Dresden-Rossendorf (HZDR), Germany, as well as

*Present address: Department of Physics and Astronomy, University of North Carolina at Chapel Hill, Chapel Hill, North Carolina 27599, USA and Triangle Universities Nuclear Laboratory, Durham, North Carolina 27708, USA.

†Present address: Institut für Kernphysik, Technische Universität Darmstadt, 64289 Darmstadt, Germany.

‡Present address: Physikalisch-Technische Bundesanstalt, 38116 Braunschweig, Germany.

using quasimonoenergetic, polarized photon beams produced at the high-intensity γ-ray source (HIγS) [4], operated by the Triangle Universities Nuclear Laboratory (TUNL) in Durham, North Carolina, USA, we observed enhanced strength on top of the low-energy tail of the GDR, for example, in $N = 50$ isotones [5], in Mo isotopes with $N = 50$ to 58 [6], and in Xe isotopes with $N = 70$ to $N = 80$ [7]. Such enhanced $E1$ strength in the excitation-energy region from about 6 to 10 MeV is considered as a pygmy dipole resonance (PDR) [8–10]. To investigate the possible influence of the PDR on cross sections and reaction rates, the experimental strength distributions were used as an input for statistical reaction-model calculations. As an example, the photoabsorption cross section deduced from (γ, n) data obtained at HIγS and the one from (γ, γ') data obtained at γELBE for ^{86}Kr were combined and used as an input for the calculation of (n, γ) reaction rates of the s-process branching-point nuclide ^{85}Kr, which provided novel information about stellar processes [11]. The experiments performed on Xe isotopes at HIγS and at γELBE revealed that the neutron excess causes the dominating effect on the development of $E1$ strength in the pygmy region, whereas the deformation plays a minor role only [7]. The experiments at HIγS using polarized photon beams allow a distinction between the $E1$ and $M1$ contributions to the photoabsorption cross sections. An investigation of ^{128}Xe and ^{134}Xe including strength in the quasicontinuum of unresolved states proved that the main part ($\approx$90%) of the photoabsorption cross section in the pygmy region is of $E1$ character, while the $M1$ cross section gives a comparably small contribution only [12]. This relation seems to change when going to lighter nuclides, such as the ones in the iron-nickel region. In ^{50}Cr [13,14], ^{52}Cr [15,16], ^{54}Cr [14], ^{56}Fe [17], and ^{58,60}Ni [18], several strong isolated $M1$ excitations have been observed. A detailed investigation of these finding requires the study of further nuclei with varing properties, such as nuclides at shell closures and within open shells. This may serve as a test of current phenomenological approximations of the $E1$ and $M1$ strength functions used as an input for statistical reaction-model calculations.

To address these issues, we initiated a study of the nuclide ^{54}Fe having a closed neutron shell ($N = 28$). In a previous NRF experiment, one $J = 1$ state at 6129 keV with a level width of $\Gamma = 27(4)$ meV was identified without parity assignment [19]. We performed experiments at γELBE at electron energies of 7.5 and 13.9 MeV to determine integrated scattering cross sections of excited states and the photoabsorption cross section including contributions from the quasicontinuum of states. Furthermore, experiments at HIγS using photon-beam energies between 5.5 and 11.4 MeV were conducted to identify individual $M1$ and $E1$ transitions in ^{54}Fe.

II. EXPERIMENTAL METHODS AND RESULTS

A. The photon-scattering method

In photon-scattering experiments, the energy- and solid-angle-integrated scattering cross section I_s of an excited state at the energy E_x is deduced from the measured intensity of the respective transition to the ground state. It can be determined relative to known integrated scattering cross sections. In the present experiments, we used the integrated scattering cross sections $I_s(E_x^{\mathrm{B}})$ of states in ^{11}B [20] and their angular correlations including mixing ratios [21] as a reference:

$$\frac{I_s(E_x)}{I_s(E_x^{\mathrm{B}})} = \left(\frac{I_\gamma(E_\gamma, \theta)}{W(E_\gamma, \theta)\Phi_\gamma(E_x)N_N} \right)$$
$$\times \left(\frac{I_\gamma(E_\gamma^{\mathrm{B}}, \theta)}{W(E_\gamma^{\mathrm{B}}, \theta)\Phi_\gamma(E_x^{\mathrm{B}})N_N^{\mathrm{B}}} \right)^{-1}. \quad (1)$$

Here, $I_\gamma(E_\gamma, \theta)$ and $I_\gamma(E_\gamma^{\mathrm{B}}, \theta)$ denote the detector-efficiency-corrected measured intensities of a considered ground-state transition at E_γ and of a ground-state transition in ^{11}B at E_γ^{B}, respectively, observed at an angle θ to the beam. $W(E_\gamma, \theta)$ and $W(E_\gamma^{\mathrm{B}}, \theta)$ describe the angular correlations of these transitions. The quantities N_N and N_N^{B} are the numbers of nuclei in the ^{54}Fe and ^{11}B targets, and $\Phi_\gamma(E_x)$ and $\Phi_\gamma(E_x^{\mathrm{B}})$ stand for the photon fluxes at the energy of the considered level and at the energy of a level in ^{11}B, respectively.

The integrated scattering cross section is related to the partial width of the ground-state transition Γ_0 according to

$$I_s = \int \sigma_{\gamma\gamma} \, dE = \left(\frac{\pi \hbar c}{E_x} \right)^2 \frac{2J_x + 1}{2J_0 + 1} \frac{\Gamma_0^2}{\Gamma}, \quad (2)$$

where $\sigma_{\gamma\gamma}$ is the elastic-scattering cross section; E_x, J_x, and Γ denote energy, spin, and total width of the excited level, respectively; and J_0 is the spin of the ground state.

The determination of the level widths is complicated by two problems. First, a considered level can be fed by transitions from higher-lying states, and second, such a level can deexcite to low-lying excited states (inelastic scattering) in addition to the deexcitation to the ground state (elastic scattering). In the case of feeding, the measured intensity of the ground-state transition is greater than the one resulting from a direct excitation only. As a consequence, the integrated scattering cross section I_{s+f} deduced from this intensity contains a portion, I_f, originating from feeding in addition to the true integrated scattering cross section I_s. In the case of inelastic scattering, inelastic and subsequent cascade transitions appear in the measured spectrum in addition to ground-state transitions. To deduce the partial width of the ground-state transition Γ_0 and the absorption cross section, the knowledge of the branching ratio $b_0 = \Gamma_0/\Gamma$ is needed.

Spins of excited states can be deduced by comparing experimental ratios of γ-ray intensities, measured at two angles, with theoretical predictions. The optimum combination includes angles of 90° and 127° because the respective ratios for the spin sequences $0 - 1 - 0$ and $0 - 2 - 0$ differ most at these angles. The expected values are $W(90°)/W(127°)_{0-1-0} = 0.74$ and $W(90°)/W(127°)_{0-2-0} = 2.15$ taking into account opening angles of 16° and 14° of the detectors placed at 90° and 127°, respectively, in the setup at γELBE.

Parities of excited states can be determined by measuring the linear polarizations of the ground-state transitions. These are deduced from experimental asymmetries of intensities

measured parallel or perpendicular to the polarization plane of the incident polarized photon beam at HIγS.

B. The target

The target consisted of 1.4984 g of iron, enriched to 99.93% in ^{54}Fe and shaped to a disk of 20 mm in diameter. In the experiments at γELBE, the target was combined with 0.300 g of boron, enriched to 99.5% in ^{11}B and also formed to a disk of 20 mm in diameter. The known integrated scattering cross sections of states in ^{11}B were used to determine the photon flux.

C. Detector response

For the determination of the integrated scattering cross sections according to Eq. (1), the efficiencies of the detectors and the photon flux are needed. The determination of the absorption cross section described in Sec. III requires in addition a correction of the experimental spectra for atomic processes induced by the impinging photons in the target material and for ambient background radiation. The detector response was simulated using the program package GEANT4 [22–24]. The reliability of the simulations was tested by comparing simulated spectra with measured ones as described, for example, in Refs. [25–28].

The absolute efficiencies of the high-purity germanium (HPGe) detectors in the setup at γELBE were determined experimentally up to 2.4 MeV from measurements with a ^{226}Ra calibration source. For interpolation, an efficiency curve calculated with GEANT4 and scaled to the absolute experimental values was used. A check of the simulated efficiency curve up to about 9 MeV was performed via various (p, γ) reactions at the HZDR Tandetron accelerator. The efficiency values deduced from these measurements agree with the simulated values within their uncertainties [29]. Similar results were obtained for the resonances at 4.44 and 11.66 MeV in ^{12}C populated in the ^{11}B(p, γ) reaction at the TUNL van-de-Graaff accelerator [30].

D. Experiments with bremsstrahlung at γELBE

The nuclide ^{54}Fe was studied in two experiments at γELBE [3]. Bremsstrahlung was produced using electron beams of 7.5 and 13.9 MeV kinetic energy. In the measurement at 7.5 MeV, the electron beam hit a niobium foil of 5 μm in thickness acting as a radiator at an average current of about 650 μA. In the measurement at 13.9 MeV, the radiator had a thickness of 12.5 μm and the average current was about 530 μA. A 10-cm-thick aluminum absorber (beam hardener) was placed behind the radiator to reduce the low-energy intensity of the bremsstrahlung spectrum in the measurement at 13.9 MeV. The photon beam, collimated by a 260-cm-long pure-aluminum collimator with a conical borehole of 8 mm in diameter at the entrance and 24 mm in diameter at the exit, impinged onto the target, placed 200 cm behind the collimator exit, with a flux of about 10^9 s^{-1} in a spot of 38 mm in diameter. Scattered photons were measured with four HPGe detectors that have an efficiency of 100% relative to an NaI detector of 7.6 cm in diameter and 7.6 cm in length.
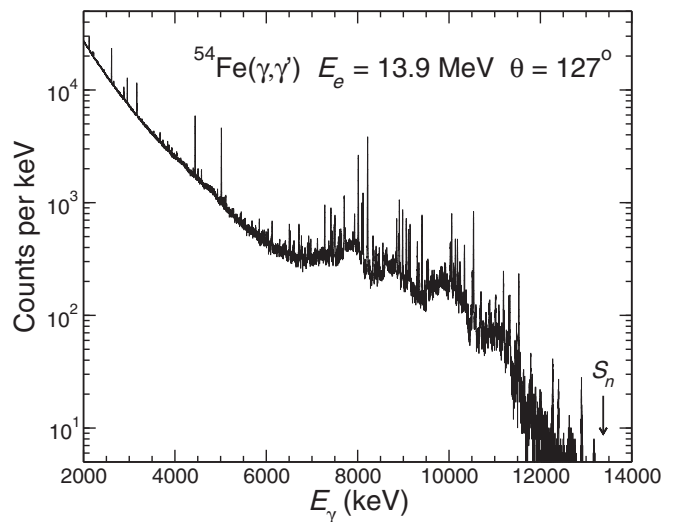

FIG. 1. Part of a spectrum of photons scattered from ^{54}Fe combined with ^{11}B, measured during the irradiation with bremsstrahlung produced by electrons of an energy of $E_e^{\text{kin}} = 13.9$ MeV. This spectrum is the sum of the spectra measured with the two detectors placed at 127° relative to the beam.

All HPGe detectors were surrounded by escape-suppression shields made of bismuth germanate scintillation detectors of 3 cm in thickness. Two HPGe detectors were placed vertically at 127° relative to the photon-beam direction and a distance of 32 cm from the target. The other two HPGe detectors were positioned in a horizontal plane at 90° to the beam and a distance of 28 cm from the target. Absorbers of 8 mm lead plus 3 mm copper were placed in front of the detectors at 90° and of 3 mm lead plus 3 mm copper in front of the detectors at 127°. Spectra of scattered photons were measured for 86 and 141 h in the experiments at 7.5 and 13.9 MeV electron energy, respectively. Part of the spectrum including events measured with the two detectors placed at 127° relative to the beam at an electron energy of 13.9 MeV is shown in Fig. 1.

The absolute photon fluxes in the two measurements at γELBE were determined from intensities and known integrated scattering cross sections of transitions in ^{11}B. For interpolation, the photon flux was calculated using a bremsstrahlung computer code [31] based on the Born approximation with Coulomb correction [32] and including an atomic screening correction [33]. In addition, the flux was corrected for the attenuation by the beam hardener. The calculated flux curves were scaled to the experimental values obtained at the energies of levels in ^{11}B. The experimental flux values and the calculated curves are shown in Fig. 2.

The measurements at two electron energies allowed us to identify inelastic transitions from high-lying levels that feed low-lying levels. Transitions found in the measurement at $E_e^{\text{kin}} = 7.5$ MeV are assumed to be ground-state transitions. Transitions additionally observed up to 7.5 MeV in the measurement at 13.9 MeV are considered as inelastic transitions from high-lying to low-lying excited states. By comparing the respective spectra, these inelastic transitions were sorted out. The remaining ground-state transitions were used to derive the
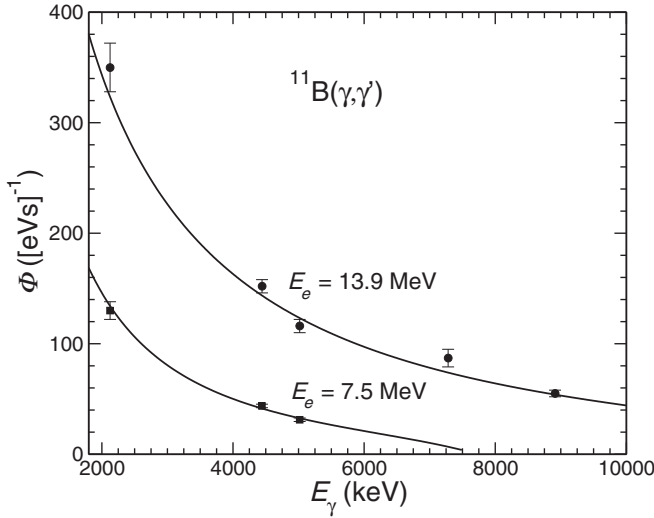
FIG. 2. Absolute photon flux on the target deduced from intensities of known transitions in ^{11}B for the measurements at $E_e =$ 7.5 MeV (squares) and $E_e = 13.9$ MeV (circles). The solid lines represent the calculated flux curves described in the text.

corresponding level energies that are listed in Table I together with spin assignments deduced from angular distributions of the ground-state transitions and with integrated scattering cross sections.

The detection limit for a 95% confidence level is defined as $A_{DL} = 2.8\sqrt{2B}$ [35], where B is the integral over a background interval of full width at half maximum (FWHM) of a nearby peak, which has been applied in similar experiments [36]. The state with the smallest I_s in Table I is the one at 5432 keV with $I_s = 1.9(3)$ eV b. At this peak, one obtains $A_{DL}/A_{PEAK} = 0.38(9)$ from the 127° spectra at γELBE, i.e., the I_s of the 5432 keV state is still more than twice the detection limit. Toward high energy, the background decreases rapidly, while FWHM increases. For the highest state given in Table I at 13 171 keV, one obtains $A_{DL}/A_{PEAK} = 0.33(9)$.

E. Experiments with monoenergetic and linearly polarized photon beams at HIγS

Monoenergetic photon beams are produced at HIγS by Compton backscattering of a high-intensity free-electron laser (FEL) beam from an intense electron beam in the TUNL storage ring. Presently, the energy of the backward-scattered photons can be tuned in a wide energy range, from about 1 to 100 MeV, by changing the energy of the electron beam and the FEL wavelength [4]. The polarization of the FEL photons, defined by the magnetic field of the undulators, is mostly preserved during the Compton backscattering due to a negligible recoil effect, leading to the production of intense photon beams with a degree of polarization of nearly 100%.

The measurements at HIγS were carried out at photon-beam energies of 5.5, 5.7, 5.9, 6.1, 6.3, 6.6, 6.8, 7.0, 7.2, 7.6, 7.9, 8.1, 8.3, 8.5, 8.7, 8.9, 9.1, 9.3, 9.5, 9.8, 10.0, 10.3, 10.6, 10.9, 11.1, and 11.4 MeV. The energy spread (FWHM) of the beam was about 3% of the energy using a 30.5-cm-long lead collimator with a cylindrical hole of 1.9 cm in diameter

TABLE I. Levels assigned to ^{54}Fe.

E_x (keV)[a]	$I_\gamma(90°)/I_\gamma(127°)$[b]	A[c]	$J_x^{\pi\,d}$	I_s (eV b)[e]
1408.5(2)[f]	1.19(10)			18.3(20)[g]
2958.5(3)[f]	1.98(26)		(2)	8.1(11)[g]
3165.9(4)[f]	1.43(22)			6.3(9)[g]
4581.7(7)[f]	1.4(5)			5.4(14)[g]
5085.0(6)	0.72(23)		1	4.1(10)
5114.1(3)	0.90(21)		(1)	4.7(7)
5431.8(7)	1.0(3)		(1)	1.9(3)
6127.8(3)	0.54(6)	−0.87(7)	1$^-$	15.0(15)[h]
6522.7(3)	0.73(12)	−0.98(3)	1$^-$	10.1(13)
6787.6(9)	0.71(26)		1	5.8(7)
6841.3(6)	0.66(27)	>0	1$^+$	6.5(17)
6914.2(9)	0.78(17)	>0	1$^+$	6.3(13)
6928.8(3)	1.01(14)		(1)	19.4(23)
6946.5(6)	1.3(3)			9.6(18)
6975.1(4)	0.55(15)		1	15.5(26)
7072.9(9)	0.9(4)		(1)	5.6(14)
7085.4(7)	0.7(3)		1	6.4(15)
7120.9(4)	1.00(18)	−0.74(18)	(1)$^-$	21.0(29)
7138.5(9)				7.4(17)
7334.8(7)				6.7(15)
7348.5(6)	0.84(27)		(1)	8.6(16)
7367.3(4)				17.4(25)
7396.0(20)				5.6(27)
7415.4(3)	1.07(7)			79(8)
7447.2(3)	0.94(12)		(1)	32(4)
7469.7(12)				9(3)
7487.4(4)	1.06(11)			42(5)
7553.3(9)	0.7(3)		1	22(7)
7631.3(4)				33(4)
7645.8(5)	1.66(18)			23.4(28)
7723.2(5)	1.25(12)			31(3)
7898.2(5)	1.07(17)			19.7(28)
7916.5(9)	1.6(4)			9.8(20)
7933.8(2)	1.09(9)			55(5)
8014.8(2)	0.74(3)	−0.93(1)	1$^-$	344(3)
8093.2(2)	0.71(5)	−0.91(7)	1$^-$	106(10)
8119.2(2)	0.73(4)	+0.95(6)	1$^+$	148(13)
8163.7(7)	0.49(28)		1	22(8)
8219.6(2)	0.72(3)	−0.91(2)	1$^-$	589(51)
8265.3(7)	1.1(3)			11.2(28)
8338.4(4)	0.77(7)	+0.92(4)	1$^+$	61(6)
8353.7(6)	0.64(10)	−0.98(7)	1$^-$	35(4)
8403.1(5)	1.07(21)			22(3)
8450.2(5)	0.74(15)	≈ -1	1$^-$	23(3)
8618.0(7)	0.63(12)	$\approx +1$	1$^+$	30(4)
8777.4(7)	0.9(4)		(1)	18(5)
8841.0(5)	1.06(17)			18.8(26)
8855.5(2)	0.69(4)	+0.98(2)	1$^+$	102(9)
8897.1(3)	0.77(5)	−0.91(8)	1$^-$	67(6)

TABLE I. *(Continued.)*

E_x (keV)[a]	$I_\gamma(90°)/I_\gamma(127°)$[b]	A[c]	J_x^{π}[d]	I_s (eV b)[e]
8930.3(7)	0.57(15)		1	17(3)
8986.0(2)	0.68(4)	+0.85(3)	1^+	142(13)
9065.2(3)	0.63(4)	+0.81(5)	1^+	130(12)
9113.1(2)	0.73(5)	+0.91(5)	1^+	94(8)
9128.9(7)	1.22(22)			13.8(23)
9149.3(2)	0.66(4)	+0.77(5)	1^+	104(9)
9307.3(3)	0.62(6)	> 0	1^+	79(8)
9342.2(4)	0.69(10)	−0.98(4)	1^-	30(4)
9410.4(2)	0.63(3)	+0.85(5)	1^+	178(16)
9472.4(10)				48(18)
9515.4(5)	0.54(11)	≈ −1	1^-	49(7)
9538.0(6)	0.41(8)	≈+1	1^+	47(7)
9908.6(6)	0.93(17)	> 0	(1^+)	38(7)
9925.3(6)	0.78(13)	> 0	1^+	38(5)
10035.5(3)	0.63(6)			93(9)
10060.5(2)	0.62(3)	>0	1^+	224(20)
10101.4(4)	0.58(7)	<0	1^-	52(6)
10119.2(5)	0.93(12)		(1)	33(4)
10140.9(2)	0.63(4)	+0.93(2)	1^+	128(12)
10185.9(3)	0.58(7)	+0.93(2)	1^+	116(14)
10195.7(11)	0.68(20)		1	33(9)
10224.2(11)	0.42(23)		1	15(4)
10240.4(5)	0.63(8)	−0.63(17)	1^-	58(7)
10250.5(6)	0.74(11)	−0.82(24)	1^-	42(6)
10339.4(2)	0.59(5)	−0.99(2)	1^-	138(13)
10376.9(9)	0.9(4)	−0.8(4)	$(1)^-$	32(9)
10487.5(8)	0.50(20)	−0.53(21)	1^-	21(8)
10510.5(4)	0.55(11)	−0.94(8)	1^-	71(11)
10538.1(2)	0.62(3)	+0.86(13)	1^+	327(29)
10590.7(7)	0.40(17)	−0.93(12)	1^-	21(6)
10701.2(4)	0.57(6)	−0.93(5)	1^-	46(5)
10802.5(14)	0.22(15)		1	26(9)
10820.4(10)	0.34(15)		1	27(8)
10880.2(7)	0.57(11)	−0.98(28)	1^-	29(4)
10891.3(7)	0.59(11)	−0.99(11)	1^-	27(4)
10926.1(7)	0.51(18)	−0.89(7)	1^-	15(3)
11021.7(6)	0.47(9)	<0	1^-	105(17)
11094.8(6)	0.54(13)		1	32(5)
11159.8(10)	0.23(15)		1	15(3)
11194.0(3)	0.55(4)	−0.97(4)	1^-	99(9)
11210.6(5)	0.47(7)	−0.89(13)	1^-	36(4)
11314.0(6)	0.65(8)	−0.82(13)	1^-	46(6)
11333.5(4)	0.55(5)	−0.84(19)	1^-	74(8)
11447.4(4)	0.72(14)		1	11.2(22)
11480.6(6)	0.74(16)	−0.89(14)	1^-	37(6)
11530.6(3)	0.63(5)	−0.79(8)	1^-	156(15)
11561.4(12)	0.43(15)		1	17(4)
11761.1(14)	1.0(4)			6.8(19)
11790.5(5)	0.73(12)		1	28(4)
11821.7(10)	0.8(3)		(1)	9.9(23)
12273.2(5)	0.60(10)		1	27(3)
12397.0(7)	0.35(11)		1	25(4)
12902.5(8)	0.33(13)		1	29(5)
13171.4(15)	0.19(9)		1	6.0(10)

[a]Excitation energy. The uncertainty of this and the other quantities in the table is given in parentheses in units of the last digit. This energy value was deduced from the γ-ray energy measured at 127° including a recoil and Doppler-shift correction.

[b]Ratio of the intensities measured at angles of 90° and 127°. The expected values for an elastic dipole transition (spin sequence $0 - 1 - 0$) and for an elastic quadrupole transition (spin sequence $0 - 2 - 0$) are 0.74 and 2.15, respectively.

[c]Azimuthal asymmetry $A = (I_{\gamma H} - I_{\gamma V})/(I_{\gamma H} + I_{\gamma V})$ of the intensities $I_{\gamma H}$ and $I_{\gamma V}$ measured with the detectors placed in a horizontal and vertical plane, respectively. A negative asymmetry indicates $E1$ radiation and a positive asymmetry indicates $M1/E2$ radiation.

[d]Spin and parity deduced from angular correlation and azimuthal asymmetry, respectively, of the ground-state transition.

[e]Energy-integrated scattering cross section. Below an excitation energy of 6.5 MeV the value was deduced from the measurement at 7.5 MeV electron energy, otherwise the value was deduced from the measurement at 13.9 MeV.

[f]This state is assumed to be a known 2^+ state [34].

[g]Value probably affected by feeding intensities.

[h]This value compares to $I_s = 7.5(11)$ eV b deduced from the level width given in Ref. [19].

positioned 60 m downstream from the collision point of the electrons with the FEL photons. The measuring time was on average about 3 h for each selected energy. The photon beam impinged onto the target with a flux of about 5×10^6 s^{-1} for the lowest energies up to 3×10^7 s^{-1} for the highest energies. Scattered photons were measured with four HPGe detectors of 60% relative efficiency, placed at polar angles of 90° to the beam, two in the vertical plane and two in the horizontal plane through the beam tube. The type of radiation ($E1$ or $M1/E2$) was deduced from a comparison of the intensities of the transitions measured at the different azimuthal angles [21,37]. In the present setup, $E1$ radiation is detected preferentially in the vertical detectors and $M1$ radiation in the horizontal detectors. As an example, spectra measured at a beam energy of 10.6 MeV are shown in Fig. 3 together with the corresponding section of the spectrum from Fig. 1. The spectra allow a clear distinction between $E1$ and $M1$ radiation. Azimuthal asymmetries $A = (I_{\gamma H} - I_{\gamma V})/(I_{\gamma H} + I_{\gamma V})$ deduced from the intensities $I_{\gamma H}$ measured in the horizontal detectors and $I_{\gamma V}$ measured in the vertical detectors are given in Table I together with the resulting parities' assignments to the emitting states. Inelastic transitions, for example, from the states in the excited energy region to the 2_1^+ state, could not be clearly identified because of the low statistics in these short measurements.

The 6523-keV peak is the smallest observed at HIγS with a definite asymmetry determination. In the spectrum of the vertical detectors at 6.6 MeV beam energy, one obtains for
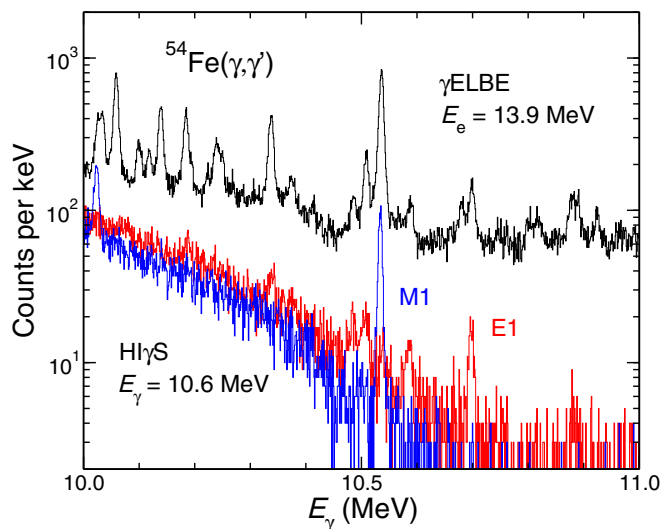
FIG. 3. Parts of spectra of photons scattered from ^{54}Fe, measured during the irradiation with a quasimonoenergetic polarized photon beam of 10.6 MeV at HIγS. The spectrum plotted in red was measured with the vertical detectors and contains $E1$ radiation, whereas the spectrum plotted in blue was measured with the horizontal detectors and contains $M1$ radiation. For comparison, the corresponding section of the spectrum measured with bremsstrahlung of $E_e = 13.9$ MeV at γELBE (cf. Fig. 1) is shown in black.

the detection limit (see Sec. II D) the relation $A_{DL}/A_{PEAK} = 0.30(4)$, compared with $A_{DL}/A_{PEAK} = 0.12(1)$ at γELBE.

III. DETERMINATION OF THE DIPOLE-STRENGTH DISTRIBUTION

The determination of the dipole-strength distribution and the related photoabsorption cross section requires the knowledge of the intensity distribution of the ground-state transitions and their branching ratios. As these cannot be derived directly from the measured spectra, we applied statistical methods to discriminate between γ rays from nuclear excitations and photons scattered by atomic processes and to disentangle the intensity distributions of elastic and inelastic transitions in the quasicontinuum of nuclear levels.

First, a spectrum of the ambient background adjusted to the intensities of the transitions from ^{40}K and ^{208}Tl decay in the in-beam spectrum was subtracted from the measured spectrum. To correct the spectrum for the detector response, spectra of monoenergetic γ rays were calculated in steps of 10 keV by using the simulation code GEANT4. Starting from the high-energy end of the experimental spectrum, the simulated spectra were subtracted sequentially (spectrum-stripping method) [38].

The background radiation produced by atomic processes in the ^{54}Fe target was obtained from a GEANT4 simulation. The simulated atomic background is compared with the response-corrected spectrum in Fig. 4. As found in previous studies [5,6,12,27,39–42] the continuum in the spectrum of γ rays scattered from ^{54}Fe is considerably higher than the background due to atomic scattering. This continuum is formed by a large number of unresolved transitions with small intensities
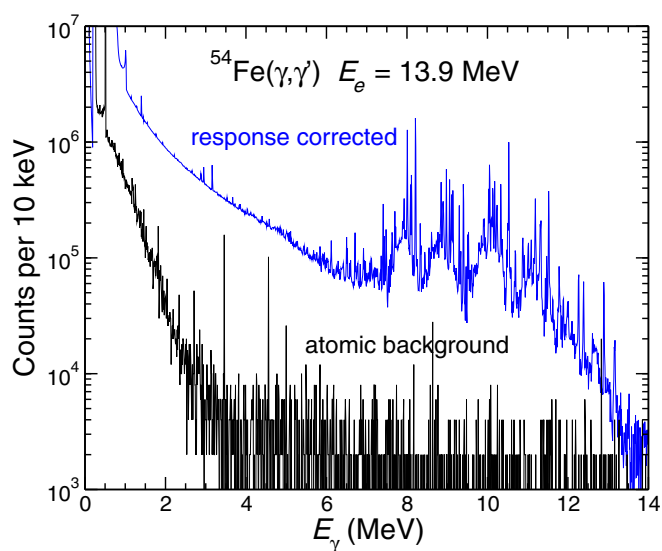

FIG. 4. Response-corrected spectrum of the two detectors placed at 127° (blue) and simulated spectrum of photons scattered from the target to the detectors by atomic processes (black).

that are a consequence of the increasing nuclear level density at high excitation energies in connection with the finite detector resolution.

The intensity distribution resulting from the subtraction of the atomic background contains ground-state (elastic) transitions and, in addition, branching (inelastic) transitions to lower-lying excited states as well as transitions from those states to the ground state (cascade transitions). The different types of transitions cannot be clearly distinguished. However, for the determination of the photoabsorption cross section and the partial widths Γ_0, the intensities of the ground-state transitions are needed. Therefore, contributions of inelastic and cascade transitions have to be subtracted from the spectra. We corrected the intensity distributions by simulating γ-ray cascades from the levels in the whole energy range using the code γDEX [28,43]. This code works analogously to the strategy of the code DICEBOX [44] developed for (n, γ) reactions, but in addition it includes also the excitation from the ground state. In the present simulations, level schemes (nuclear realizations) including states with $J = 0, ..., 5$ were created. For the low-energy part of the level scheme below 3.5 MeV, experimentally known levels were taken into account. Fluctuations of the partial widths were treated by applying the Porter-Thomas distribution [45]. Level densities were calculated by using the constant-temperature model [46] with the parameters $T = 1.42(3)$ MeV and $E_0 = 0.04(11)$ MeV adjusted to experimental level densities [47]. In the individual nuclear realizations, the values of T and E_0 were varied randomly within a Gaussian distribution with a σ corresponding to the uncertainties given in Ref. [47]. The parity distribution of the level densities was modeled according to the information given in Ref. [48].

The first inputs for the photon strength function simulations were assumed to be Lorentz-shaped. For the $E1$ strength a combination of three Lorentz functions (TLO),
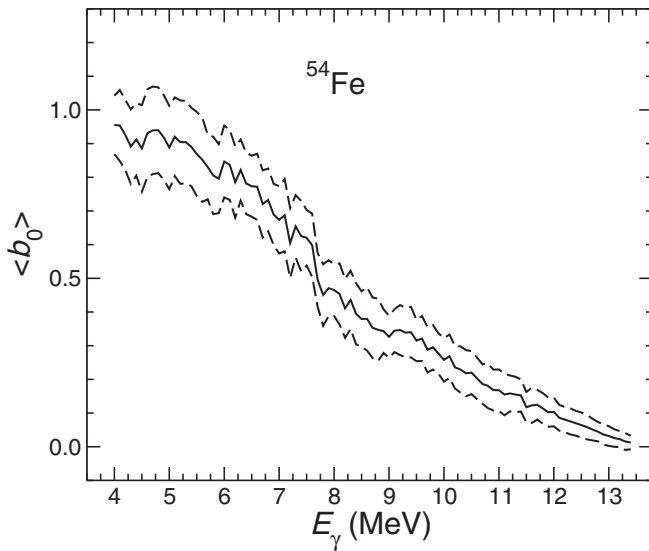
FIG. 5. Average branching ratios (solid line) with their uncertainty ranges (dashed lines) resulting from the simulations of statistical γ-ray cascades up to S_n as described in the text.

with parameters as described in Refs. [49,50], was used with deformation parameters of $\beta_2 = 0.2$ [51] and $\gamma = 30°$ [52]. The parameters for the $M1$ and $E2$ strengths were taken from global parametrizations of $M1$ spin-flip resonances and $E2$ isoscalar resonances, respectively [53]. Spectra of γ-ray cascades were generated for groups of levels in 100-keV bins. Starting from the high-energy end of the experimental spectrum, which contains ground-state transitions only, the simulated intensities of the ground-state transitions were normalized to the experimental ones in the considered bin. The intensity distribution of the branching transitions was subtracted from the experimental spectrum. Applying this procedure step-by-step for each energy bin moving toward the low-energy end of the spectrum, one obtains the intensity distribution of the ground-state transitions. Simultaneously, the branching ratios $b_0(E)$ of the ground-state transitions are deduced for each energy bin ΔE. In an individual nuclear realization, the branching ratio $b_0(E)$ is calculated as the ratio of the sum of the intensities of the ground-state transitions from all levels in ΔE to the total intensity of all transitions depopulating those levels to any low-lying levels including the ground state [5–7,28,42,43]. Average branching ratios derived from the present cascade simulations are illustrated in Fig. 5. By dividing the summed intensities $N(E)$ in a bin of the experimental intensity distribution of the ground-state transitions with the corresponding branching ratio and transforming the intensities to a cross section analogous to Eq. (1), we obtain the absorption cross section in each bin as $\sigma_\gamma(E) = \sigma_{\gamma\gamma}(E)/b_0(E)$ for each nuclear realization. The uncertainty of the intensity in an energy bin was deduced as $\delta N(E) = \sqrt{N(E)} + \sum [\sqrt{N(E' > E)} b(E' \to E)]$, where $b(E' \to E)$ is the branching intensity from bin E' to bin E. Finally, the absorption cross sections of each bin were obtained by averaging over the values of the nuclear realizations. The simulations were performed iteratively. The strength function

obtained from an iteration step was used as the input for the next step. The iteration was stopped when the input strength function and the output strength function were in agreement within their uncertainties. The cross section obtained in the last (ninth) iteration step is taken as the final absorption cross section. The uncertainties of the cross-section values include statistical uncertainties of the spectrum, the given uncertainty of the efficiency, uncertainties of the flux resulting from the integrated cross sections of the ^{11}B levels, and the mentioned uncertainties of the level-density parameters.

Toward low energy, the uncertainties increase due to the use of the spectrum-stripping method and the cross sections do not converge. Therefore, cross sections cannot be determined below an excitation energy of 7 MeV in the high-energy measurement. To obtain values at lower energies, the same procedure was applied to the low-energy measurement.

IV. DISCUSSION

The experimental photoabsorption cross sections resulting from the procedure just described for the (γ, γ') data obtained from the measurements at $E_e = 7.5$ and 13.9 MeV are listed in Tables II and III and are graphed in Fig. 6 together with the experimental cross section for the (γ, n) reaction [54]. The (γ, γ') cross section is characterized by several peaks rather than by a smooth curve. Most of these peaks correspond to the prominent excitations seen in Table I and Figs. 1 and 4, which appear on top of the quasicontinuum. This structure resembles the ones found for other nuclides near closed shells, such as the $N = 50$ isotones [5,6,26,55], whereas the absorption cross sections of open-shell nuclides are rather smooth curves, for example, the ones in ^{74}Ge [39], ^{128}Xe [12], and ^{181}Ta [42]. In addition to the experimental data, the TLO with the parameters just mentioned and the photoabsorption cross section given in the latest TALYS-based evaluated nuclear data library (TENDL-2019) [56] are displayed. For the latter, the strength of the GDR used as an input for the TALYS code [57] was scaled with a factor of 1.45 [56], which leads to large values compared to the (γ, n) data and the TLO. The TENDL cross section is the sum of the ones of various reaction channels, which are shown in Fig. 7. The (γ, γ') cross section is predicted with magnitudes comparable with the experimental ones, neglecting, however, the pronounced resonancelike structures found in the experiment. The (γ, p) channel dominates the total cross section from about 12 MeV up to about 25 MeV in this $N = Z + 2$ nuclide. The predicted (γ, n) cross section underestimates the experimental one shown in Fig. 6 by a factor of about 2.5 at its maximum and is also considerably smaller than the predicted (γ, p) cross section, which dominates the GDR in the region of its maximum.

The peaks in the experimental (γ, γ') cross section are caused by prominent transitions from 1^+ as well as 1^- states. This is similar to the characteristics of other nuclides in this mass region as mentioned in Sec. I, whereas the structures of nuclides around $N = 50$ include exclusively strong excitations of 1^- states. The relation between $E1$ and $M1$ strength in ^{54}Fe can be analyzed for the transitions from states with parity assignments given in Table I. The summed integrated

TABLE II. Absorption cross section deduced from the present (γ, γ') experiment at $E_e = 7.5$ MeV.

E_γ (MeV)	σ (mb)[a]
4.3	0.16(4)
4.4	0.24(8)
4.5	0.017(9)
4.6	0.31(15)
4.9	0.50(5)
5.0	0.33(10)
5.1	0.49(8)
5.2	0.18(5)
5.3	0.15(3)
5.4	0.21(5)
5.5	0.18(8)
5.7	0.26(4)
5.8	0.12(6)
5.9	0.12(5)
6.0	0.41(18)
6.1	0.70(27)
6.2	0.25(3)
6.3	0.53(7)
6.4	0.45(8)
6.5	1.04(10)
6.6	0.45(4)
6.7	0.60(5)
6.8	0.82(5)
6.9	0.63(8)
7.0	0.44(5)
7.1	0.72(5)
7.2	0.49(4)
7.3	0.75(5)
7.4	1.58(8)
7.5	1.19(7)

[a]Absorption cross section resulting from the experimental intensity distribution including the quasicontinuum, corrected for branching intensities and branching ratios obtained from γ-ray cascade simulations. The uncertainties include statistical uncertainties of the included intensities as described in Sec. III, a 5% uncertainty of the detector efficiency, and uncertainties of the photon flux based on the uncertainties of the cross sections in ^{11}B. Systematic uncertainties of strength-function and level-density models can cause additional uncertainties of up to about 20% not included here.

scattering cross section of all definite and tentative 1^- states in Table I amounts to $\sum I_s(1^-) = 2394(65)$ eV b and that of all 1^+ states amounts to $\sum I_s(1^+) = 1999(53)$ eV b. The contribution of $M1$ strength to the total strength is hence about 45% and that of $E1$ strength is about 55%. Reduced transition strengths $B(E1)$ and $B(M1)$ were deduced assuming branching ratios $b_0 = 1$ for the ground-state transitions, because transitions from $J = 1$ states to the 2_1^+ state, which are expected to be the most intense branching transitions other than the ground-state transitions, were not clearly identified in the respective spectra measured at HIγS. The intensities of the weakly visible $2_1^+ \to 0_1^+$ transition have not been used to estimate branching ratios because the 2_1^+ state may also collect feeding intensities from other states simultaneously excited with the considered one by a given photon beam of up

TABLE III. Absorption cross section deduced from the present (γ, γ') experiment at $E_e = 13.9$ MeV.

E_γ (MeV)	σ (mb)[a]
7.0	1.1(8)
7.2	3.3(31)
7.3	1.6(8)
7.4	1.2(8)
7.5	2.1(13)
7.7	2.6(19)
7.8	3.6(14)
8.1	5.8(41)
8.2	12.2(22)
8.3	2.9(8)
8.4	3.3(7)
8.5	3.7(8)
8.6	6.7(17)
8.7	3.6(9)
8.8	3.6(11)
8.9	4.2(13)
9.0	14.8(34)
9.1	8.1(16)
9.2	7.8(13)
9.3	4.6(8)
9.4	11.0(25)
9.5	4.1(13)
9.6	6.7(10)
9.7	4.5(13)
9.8	5.9(8)
9.9	8.4(10)
10.0	10.9(9)
10.1	17.5(14)
10.2	14.4(11)
10.3	11.6(9)
10.4	8.9(7)
10.5	18.0(13)
10.6	6.6(6)
10.7	7.6(6)
10.8	7.9(6)
10.9	9.5(9)
11.0	10.2(8)
11.1	10.7(8)
11.2	12.4(7)
11.3	12.6(6)
11.4	7.6(5)
11.5	14.0(11)
11.6	8.5(7)
11.7	6.8(7)
11.8	9.4(9)
11.9	9.5(9)
12.0	8.4(9)
12.1	7.7(9)
12.2	7.3(8)
12.3	9.7(11)
12.4	8.9(10)
12.5	7.4(10)
12.6	8.0(10)
12.7	9.3(12)
12.8	6.1(9)
12.9	10.7(13)
13.0	7.3(11)

TABLE III. *(Continued.)*

E_γ (MeV)	σ (mb)[a]
13.1	5.4(9)
13.2	9.8(13)
13.3	6.2(11)
13.4	5.5(9)

[a]Absorption cross section resulting from the experimental intensity distribution including the quasicontinuum, corrected for branching intensities and branching ratios obtained from γ-ray cascade simulations. The uncertainties include statistical uncertainties of the included intensities as described in Sec. III, a 5% uncertainty of the detector efficiency, and uncertainties of the photon flux based on the uncertainties of the cross sections in ^{11}B. Systematic uncertainties of strength-function and level-density models can cause additional uncertainties of up to about 20% not included here.

FIG. 7. Photoabsorption cross section of ^{54}Fe (black line) together with the partial cross sections for the reaction channels (γ, γ') (red line), (γ, n) (green line), and (γ, p) (blue line) taken from the TENDL-2019 library.

to about 300 keV energy spread at the highest energies. The $B(E1)$ and $B(M1)$ values determined in this way are given in Tables IV and V, respectively. The summed strengths result in $\sum B(E1) = 0.0215(6)\, e^2\, \text{fm}^2$ and $\sum B(M1) = 1.59(4)\mu_N^2$. Note that these summed strengths are not the full strengths because the transitions without parity assignments in Table I are not included. Furthermore, unobserved transitions in the quasicontinuum contribute to the summed strengths as well. Nevertheless, these summed strengths are of magnitudes similar to the ones found for ^{50}Cr [13] and for the $N = 28$ isotone ^{52}Cr [15,16]. The distribution of $M1$ strength is compared with predictions of shell-model calculations in the following.
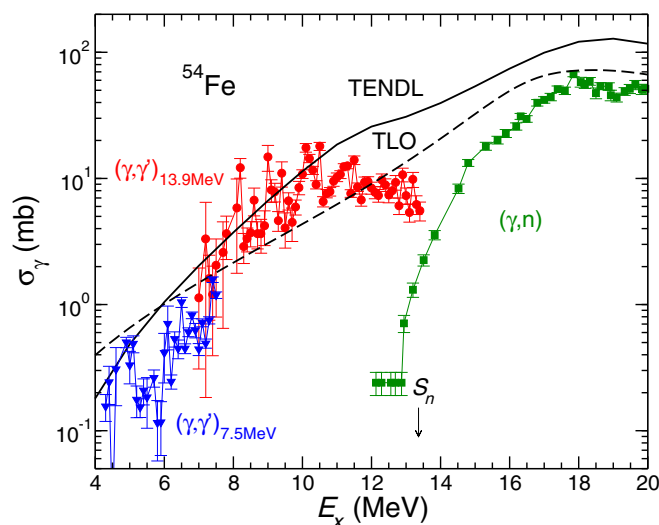

FIG. 6. Photoabsorption cross sections of ^{54}Fe resulting from the present (γ, γ') experiments at $E_e = 7.5$ MeV (blue triangles) and $E_e = 13.9$ MeV (red circles), from (γ, n) data taken from Ref. [54] (green squares), from calculations using the TALYS code as given in the TENDL-2019 library (black solid line), and from the TLO with parameters given in the text (black dashed line).
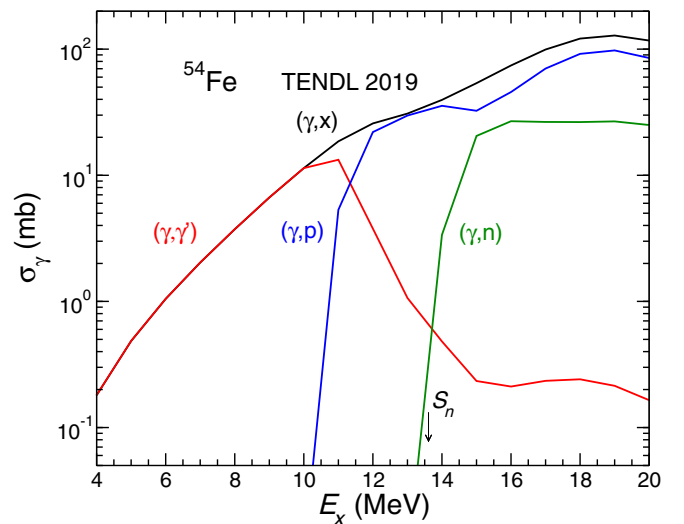
V. SHELL-MODEL CALCULATIONS

Shell-model calculations for ^{54}Fe were carried out with the GX1A Hamiltonian [58,59] for the fp shell using the code NUSHELLX@MSU [60]. The model space included the proton and neutron orbits $(0f_{7/2}, 1p_{3/2}, 0f_{5/2}, 1p_{1/2})$ without limits in occupation numbers. The calculations were performed for the lowest 120 states with $J^\pi = 1^+$. Reduced transition strengths $B(M1, 1^+ \to 0_1^+)$ were calculated using effective g factors of $g_s^{\text{eff}} = 0.74g_s^{\text{free}}$ [61]. The experimental $B(M1, 1^+ \to 0_1^+)$ values given in Table V are compared with calculated ones in Fig. 8. Out of the 120 calculated values, only the 53 values greater than $0.005\mu_N^2$ are shown. This lower limit corresponds roughly to the smallest experimental values. The first calculated 1^+ state appears at 4.560 MeV, whereas the first experimental state with a 1^+ assignment is the one at 6.841 MeV (cf. Table I). However, one or more of the states between 5.0 and 5.5 MeV, which were not covered by the experiments at HIγS, may also have spin and parity 1^+. The running sums of the $B(M1)$ values are graphed in Fig. 9. Both the experimental and calculated curves show a steplike behavior caused by strong peaks in the $B(M1)$ distributions. The steps of the calculated distribution appear by about 0.5 MeV lower in energy than the experimental ones. The summed strength $\sum B(M1) = 1.76\mu_N^2$ of the calculated values greater than $0.005\,\mu_N^2$ between $E_\gamma = 6.8$ and 10.6 MeV exceeds the upper limit of the experimental value of $\sum B(M1) = 1.59(4)\mu_N^2$ by about 8%. This relation resembles the one found for the isotone ^{50}Cr [16]. Possible reasons for the difference are that some of the states with unknown parity in Table I may be 1^+ states that are not taken into account in this comparison or may be unobserved branching transitions.

TABLE IV. Experimental reduced $E1$ transition strengths.

E_γ (MeV)	$B(E1, 1^- \to 0_1^+)$ $(10^{-4}\ e^2\ \text{fm}^2)$[a]
6.128	2.03(20)
6.523	1.28(17)
7.121	2.4(3)
8.015	35.6(3)
8.093	10.8(10)
8.220	59(5)
8.354	3.5(4)
8.450	2.25(29)
8.897	6.2(6)
9.342	2.7(4)
9.515	4.3(6)
10.101	4.3(5)
10.240	4.7(6)
10.250	3.4(5)
10.339	11.1(10)
10.377	2.6(7)
10.488	1.7(6)
10.510	5.6(9)
10.591	1.6(5)
10.701	3.6(4)
10.880	2.2(3)
10.891	2.0(3)
10.926	1.14(23)
11.022	7.9(13)
11.194	7.3(7)
11.211	2.7(3)
11.314	3.4(4)
11.334	5.4(6)
11.481	2.7(4)
11.531	11.2(11)

[a]Value obtained from the I_s of the corresponding state given in Table I, using the relation $B(E1) = 0.000\,955\ (\Gamma_0/\text{meV})/(E_\gamma/\text{meV})^3$ and Eq. (2) with $\Gamma_0/\Gamma = 1$. The uncertainty of the $B(E1)$ value was percentagewise deduced from that of I_s.

TABLE V. Experimental reduced $M1$ transition strengths.

E_γ (MeV)	$B(M1, 1^+ \to 0_1^+)$ $(10^{-2}\ \mu_N^2)$[a]
6.841	0.71(19)
6.914	0.68(14)
8.119	13.7(12)
8.338	5.5(5)
8.618	2.6(3)
8.856	8.6(7)
8.986	11.9(11)
9.065	10.8(10)
9.113	7.7(7)
9.149	8.5(7)
9.307	6.4(6)
9.410	14.2(13)
9.538	3.7(6)
9.909	2.9(5)
9.925	2.9(4)
10.060	16.7(15)
10.141	9.5(9)
10.186	8.6(10)
10.538	23.3(21)

[a]Value deduced from the I_s of the corresponding state given in Table I, using the relation $B(M1) = 0.0866\ (\Gamma_0/\text{meV})/(E_\gamma/\text{meV})^3$ and Eq. (2) with $\Gamma_0/\Gamma = 1$. The uncertainty of the $B(M1)$ value was percentagewise deduced from that of I_s.

and neutrons in Fig. 10. The states are lower in energy in the full configuration space than those in the truncated space. For example, the energy of the 2_1^+ state changes from 1.467 MeV in the limited space to 1.449 MeV in the full space and the $B(E2, 2_1^+ \to 0_1^+)$ value changes from 108 to 149 e^2 fm^4, whereas the experimental values are $E(2_1^+) = 1.408$ MeV and $B(E2, 2_1^+ \to 0_1^+) = 135(4)\ e^2$ fm^4 [34]. In the considered energy range up to 10.6 MeV, there are 40 1^+ states calculated

To get an impression about the fraction of orbital and spin contributions to the $B(M1)$ values, calculations with $g_s^\pi = 0.001$ and $g_s^\nu = -0.001$ were carried out. The ratios of the values with and without spin contribution scatter over 8 orders of magnitude for the individual transitions, reaching from almost exclusive spin contributions over dominating orbital contributions $[B(M1)/B(M1)_{g_s=0} \approx 1]$ to values smaller than 1 in cases of destructive superposition of orbital and spin parts. There is no clear tendency of these values with varying energy.

In earlier shell-model studies of ^{54}Fe [62] and of the neighboring isotope ^{56}Fe [63] using the code NUSHELLX, a truncated model space was applied to make the calculations feasible for a greater spin range and hence a much bigger number of transitions. The lowest 40 states with $J^\pi = 2^+$ calculated with a truncated model space including the proton orbits $(0f_{7/2})^{6-l}(1p_{3/2}, 0f_{5/2}, 1p_{1/2})^l$, with $l = 0$, 1, and 2, and the neutron orbits $(0f_{7/2})^{8-m}(1p_{3/2}, 0f_{5/2}, 1p_{1/2})^m$, with $m = 0$, 1, and 2, are compared with the ones obtained from the present calculations including the full fp shell for protons
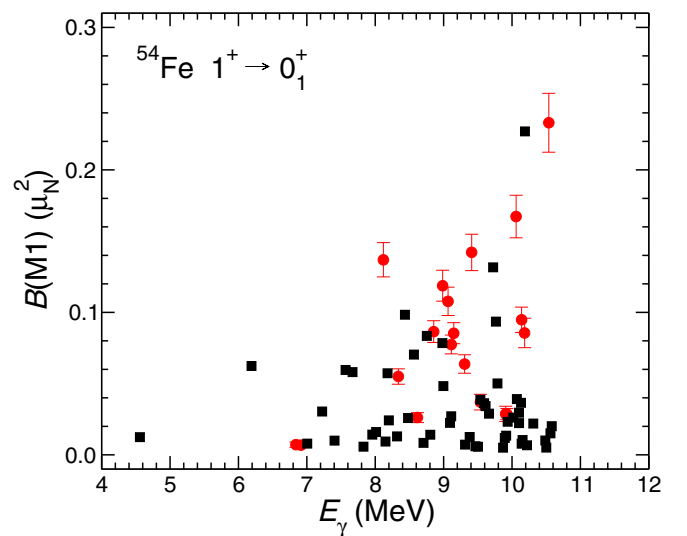

FIG. 8. Experimental $B(M1, 1^+ \to 0_1^+)$ values (red circles) and calculated values $B(M1, 1^+ \to 0_1^+) > 0.005\mu_N^2$ from the lowest 120 1^+ states (black squares).
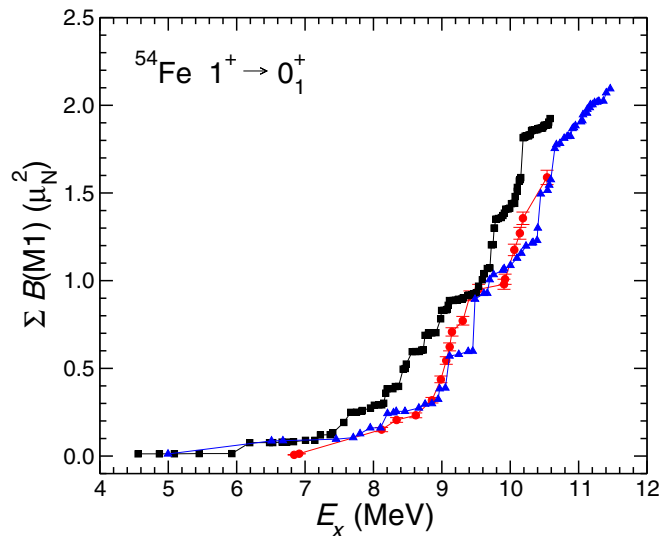
FIG. 9. Running sums $\sum B(M1, 1^+ \rightarrow 0_1^+)$ of experimental (red circles) and calculated values (black squares). Also shown are the values obtained in a truncated model space (blue triangles) discussed in the text.

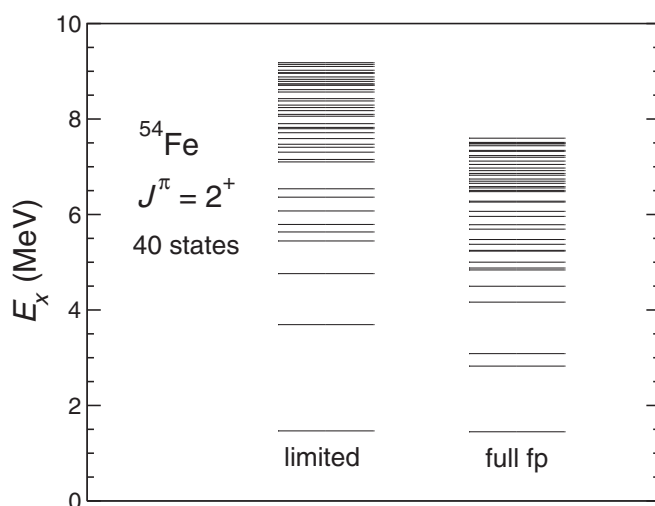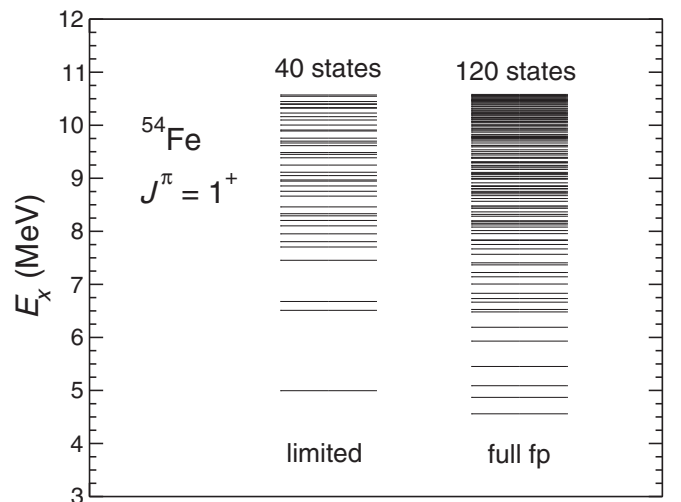FIG. 11. Energies of the lowest 40 states with $J^\pi = 1^+$ up to 10.6 MeV calculated in a model space with limited occupation numbers and the 120 states up to 10.6 MeV in the full fp space.

in the limited space, but 120 in the full space, which are compared in Fig. 11. This shows that the $M1$ strength is shifted down by almost 1 MeV in the full model space compared to the truncated model space. The running sum $\sum B(M1, 1^+ \rightarrow 0_1^+)$ including the lowest 65 states obtained with the limited space is also shown in Fig. 9. The lowering of states in the full space compared with the ones in the truncated space is reflected by a shift of the steps toward low energy. The curves shown in Fig. 9 suggest a better agreement of the experimental running sum with the one in the truncated space compared to the one in the full space. One must, however, be aware that the experimental strengths are not complete and

the strengths from the truncated space are less reliable than the ones from the full space.

As an alternative description, the $B(M1)$ distribution in ^{54}Fe was also computed in the full fp shell with the Lenzi-Nowacki-Poves-Sieja interaction [64] using the code ANTOINE [65], employing the Lanczos strength-function method with 300 iterations. A quenching factor of 0.75 was applied on the spin part of the magnetic operator. This calculation predicts the first 1^+ state at 5.0 MeV with a $B(M1, 1^+ \rightarrow 0_1^+)$ value of $0.014 \, \mu_N^2$. There are 31 states located below 10.6 MeV and the summed strength from 6.8 to 10.6 MeV amounts to $\sum B(M1) = 2.05 \mu_N^2$, being even larger than that from the GX1A shell-model calculation and thus exceeding the experimental value by about 30%.

VI. SUMMARY

The dipole-strength distribution in ^{54}Fe up to the neutron-separation energy was studied in photon-scattering experiments at the γELBE facility using bremsstrahlung at two different electron energies and at the HIγS facility using quasimonoenergetic photon beams of 26 photon energies. About 100 levels were identified. Spins $J = 1$ were deduced from angular correlations of ground-state transitions measured at γELBE and the parities of states were determined from azimuthal asymmetries of intensities measured at HIγS. The intensity distribution obtained from the measured spectra after a correction for detector response and a subtraction of atomic background in the target contains a continuum part in addition to the resolved peaks, which was included in the determination of the photoabsorption cross section. An assignment of inelastic transitions to particular levels, and thus the determination of branching ratios, was in general not possible. To get information about the intensities of inelastic transitions to low-lying levels we have applied statistical methods. By means of simulations of γ-ray cascades,

FIG. 10. Energies of the lowest 40 states with $J^\pi = 2^+$ calculated in a model space with limited occupation numbers and in the full fp space.

intensities of branching transitions were estimated and subtracted from the experimental intensity distribution and the intensities of ground-state transitions could be corrected in average for their branching ratios. In this way, a continuous photoabsorption cross section was derived for the energy range from about 4 MeV up to the neutron threshold at 13.3 MeV, which can be combined with the (γ, p) and (γ, n) cross sections toward higher energies. The data show that the $M1$ strength amounts to about 45% and the $E1$ strength to about 55% of the strength in the resolved transitions, which compares to the findings for neighboring nuclides. This contribution of $M1$ strength is considerably higher than in heavier nuclides, which are dominated by up to more than 90% of $E1$ strength in the considered energy region. Consequently, the phenomenological parametrizations of $M1$ strength as used in statistical reaction-model calculations may be reconsidered for nuclides in the mass-60 region. The experimental $B(M1)$ values were compared with predictions of shell-model calculations. Most of the calculated $B(M1, 1^+ \rightarrow 0_1^+)$ values are dominated by spin contributions.

[1] T. Kawano *et al.*, Nucl. Data Sheets **163**, 109 (2020).

[2] S. Goriely *et al.*, Eur. Phys. J. A **55**, 172 (2019).

[3] R. Schwengner *et al.*, Nucl. Instrum. Methods Phys. Res., Sect. A **555**, 211 (2005).

[4] H. R. Weller, M. W. Ahmed, H. Gao, W. Tornow, Y. K. Wu, M. Gai, and R. Miskimen, Prog. Part. Nucl. Phys. **62**, 257 (2009).

[5] R. Schwengner *et al.*, Phys. Rev. C **87**, 024306 (2013).

[6] G. Rusev *et al.*, Phys. Rev. C **79**, 061302(R) (2009).

[7] R. Massarczyk *et al.*, Phys. Rev. Lett. **112**, 072501 (2014).

[8] G. A. Bartholomew, E. D. Earle, A. J. Ferguson, J. W. Knowles, and M. A. Lone, Adv. Nucl. Phys. **7**, 229 (1973).

[9] D. Savran, T. Aumann, and A. Zilges, Prog. Part. Nucl. Phys. **70**, 210 (2013).

[10] A. Bracco, E. G. Lanza, and A. Tamii, Prog. Part. Nucl. Phys. **106**, 360 (2019).

[11] R. Raut *et al.*, Phys. Rev. Lett. **111**, 112501 (2013).

[12] R. Massarczyk, G. Rusev, R. Schwengner, F. Dönau, C. Bhatia, M. E. Gooden, J. H. Kelley, A. P. Tonchev, and W. Tornow, Phys. Rev. C **90**, 054310 (2014).

[13] H. Pai *et al.*, Phys. Rev. C **93**, 014318 (2016).

[14] P. C. Ries *et al.*, Phys. Rev. C **100**, 021301(R) (2019).

[15] T. Shizuma, T. Hayakawa, I. Daito, H. Ohgaki, S. Miyamoto, and F. Minato, Phys. Rev. C **96**, 044316 (2017).

[16] J. Wilhelmy *et al.*, Phys. Rev. C **98**, 034315 (2018).

[17] T. Shizuma, T. Hayakawa, H. Ohgaki, H. Toyokawa, T. Komatsubara, N. Kikuzawa, T. Inakura, M. Honma, and H. Nakada, Phys. Rev. C **87**, 024301 (2013).

[18] M. Scheck *et al.*, Phys. Rev. C **87**, 051304(R) (2013).

[19] H. Lancman, R. J. Sparks, and C. Van Der Leun, Nucl. Phys. A **257**, 29 (1976).

[20] F. Ajzenberg-Selove, Nucl. Phys. A **506**, 1 (1990).

[21] G. Rusev, A. P. Tonchev, R. Schwengner, C. Sun, W. Tornow, and Y. K. Wu, Phys. Rev. C **79**, 047601 (2009).

[22] S. Agostinelli *et al.*, Nucl. Instrum. Methods Phys. Res., Sect. A **506**, 250 (2003).

[23] J. Allison *et al.*, IEEE Trans. Nucl. Sci. **53**, 270 (2006).

[24] J. Allison *et al.*, Nucl. Instrum. Methods Phys. Res., Sect. A **835**, 186 (2016).

[25] G. Rusev, Dissertation, Technische Universität, Dresden, 2007, Report FZD-478, http://www.hzdr.de/publications/010008/10008.pdf.

[26] R. Schwengner *et al.*, Phys. Rev. C **76**, 034321 (2007).

[27] G. Rusev *et al.*, Phys. Rev. C **77**, 064321 (2008).

[28] R. Massarczyk *et al.*, Phys. Rev. C **86**, 014319 (2012).

[29] E. Trompler, Diploma thesis, Technische Universität, Dresden, 2009, Report FZD-523, http://www.hzdr.de/publications/013364/13364.pdf.

[30] S. Carson, C. Iliadis, J. Cesaratto, A. Champagne, L. Downen, M. Ivanovic, J. Kelley, R. Longland, J. R. Newton, G. Rusev, and A. P. Tonchev, Nucl. Instrum. Methods Phys. Res., Sect. A **618**, 190 (2010).

[31] E. Haug, Radiat. Phys. Chem. **77**, 207 (2008).

[32] G. Roche, C. Ducos, and J. Proriol, Phys. Rev. A **5**, 2403 (1972).

[33] F. Salvat, J. D. Martinez, R. Mayol, and J. Parellada, Phys. Rev. A **36**, 467 (1987).

[34] Y. Dong and H. Junde, Nucl. Data Sheets **121**, 1 (2014).

[35] R. Jenkins, R. W. Gould, and D. Gedke, *Quantitative X-Ray Spectroscopy* (Dekker, New York, 1995).

[36] E. Kwan *et al.*, Phys. Rev. C **83**, 041601(R) (2011).

[37] N. Pietralla, Z. Berant, V. N. Litvinenko, S. Hartman, F. F. Mikhailov, I. V. Pinayev, G. Swift, M. W. Ahmed, J. H. Kelley, S. O. Nelson, R. Prior, K. Sabourov, A. P. Tonchev, and H. R. Weller, Phys. Rev. Lett. **88**, 012502 (2001).

[38] A. K. Furr, E. L. Robinson, and C. H. Robins, Nucl. Instrum. Methods **63**, 205 (1968).

[39] R. Massarczyk *et al.*, Phys. Rev. C **92**, 044309 (2015).

[40] A. Makinaga *et al.*, Phys. Rev. C **94**, 044304 (2016).

[41] T. Shizuma *et al.*, Phys. Rev. C **98**, 064317 (2018).

[42] A. Makinaga *et al.*, Phys. Rev. C **90**, 044301 (2014).

[43] G. Schramm *et al.*, Phys. Rev. C **85**, 014311 (2012).

[44] F. Bečvář, Nucl. Instrum. Methods Phys. Res., Sect. A **417**, 434 (1998).

[45] C. E. Porter and R. G. Thomas, Phys. Rev. **104**, 483 (1956).

[46] A. Gilbert and A. G. W. Cameron, Can. J. Phys. **43**, 1446 (1965).

[47] T. von Egidy and D. Bucurescu, Phys. Rev. C **80**, 054310 (2009).

[48] S. I. Al-Quraishi, S. M. Grimes, T. N. Massey, and D. A. Resler, Phys. Rev. C **67**, 015803 (2003).

[49] A. R. Junghans, G. Rusev, R. Schwengner, A. Wagner, and E. Grosse, Phys. Lett. B **670**, 200 (2008).

[50] E. Grosse, A. R. Junghans, and R. Massarczyk, Eur. Phys. J. A **53**, 225 (2017).

[51] S. Raman, C. W. Nestor, Jr., and P. Tikkanen, At. Data Nucl. Data Tables **78**, 1 (2001).

[52] J.-P. Delaroche, M. Girod, J. Libert, H. Goutte, S. Hilaire, S. Péru, N. Pillet, and G. F. Bertsch, Phys. Rev. C **81**, 014303 (2010).

[53] R. Capote *et al.*, Nucl. Data Sheets **110**, 3107 (2009).

[54] J. W. Norbury, M. N. Thompson, K. Shoda, and H. Tsubota, Aust. J. Phys. **31**, 471 (1978).

[55] R. Schwengner *et al.*, Phys. Rev. C **78**, 064314 (2008).

[56] A. J. Koning, D. Rochman, J. Sublet, N. Dzysiuk, M. Fleming, and S. van der Marck, Nucl. Data Sheets **155**, 1 (2019).

[57] A. J. Koning and D. Rochman, Nucl. Data Sheets **113**, 2841 (2012), and references therein.

[58] M. Honma, T. Otsuka, B. A. Brown, and T. Mizusaki, Phys. Rev. C **69**, 034335 (2004).

[59] M. Honma, T. Otsuka, B. A. Brown, and T. Mizusaki, Eur. Phys. J. A **25**, 499 (2005).

[60] B. A. Brown and W. D. M. Rae, Nucl. Data Sheets **120**, 115 (2014).

[61] M. Honma, T. Otsuka, T. Mizusaki, M. Hjorth-Jensen, and B. A. Brown, J. Phys.: Conf. Ser. **20**, 7 (2005).

[62] R. Schwengner and G. Rusev, Phys. Rev. C **100**, 054320 (2019).

[63] B. A. Brown and A. C. Larsen, Phys. Rev. Lett. **113**, 252502 (2014).

[64] S. M. Lenzi, F. Nowacki, A. Poves, and K. Sieja, Phys. Rev. C **82**, 054301 (2010).

[65] E. Caurier and F. Nowacki, Acta Phys. Pol., B **30**, 705 (1999).